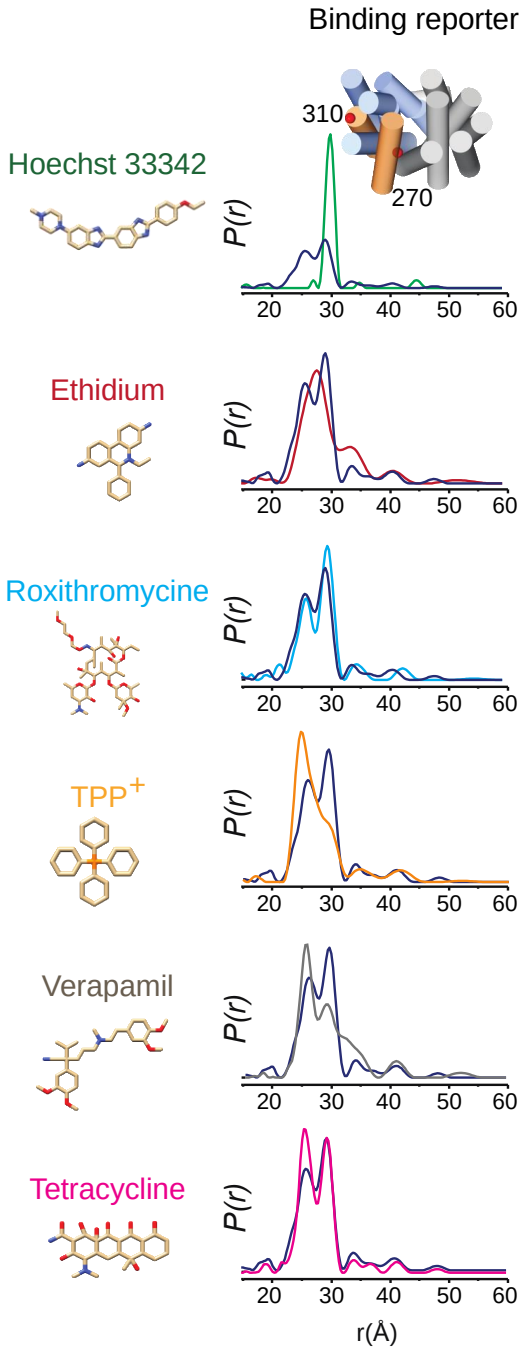

Supplementary Figure 1. Binding of different substrates to LmrP does not induce a large conformational change in the binding pocket. Limited variations in distance distribution are observed when comparing LmrP in the apo state (blue) and in the presence of Hoechst 33342 (green), ethidium bromide (red), roxithromycin (cyan), TPP^+ (yellow), verapamil (grey) and tetracycline (magenta), using one probe on the extracellular face and one within the binding pocket. Distributions were normalised. Interspin distance is denoted by *r*, with *P(r)* indicating the distance probability.

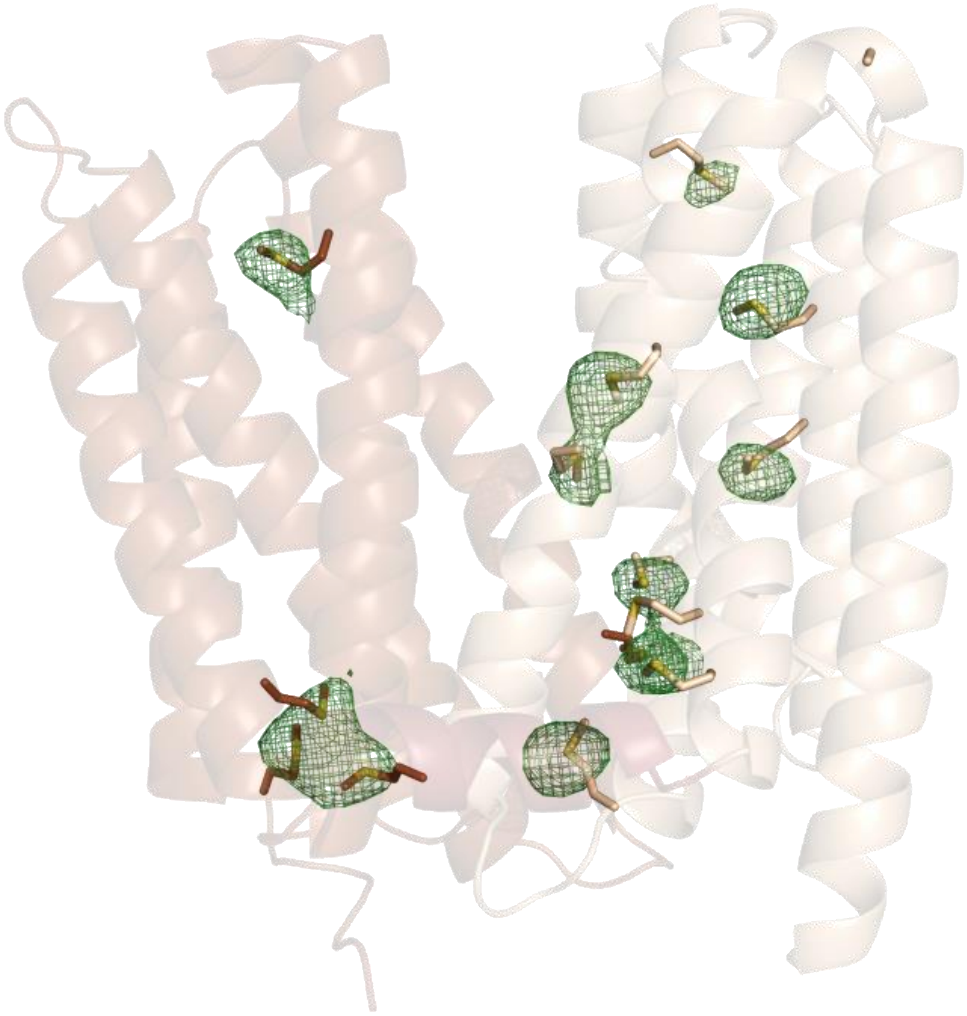

Supplementary Figure 2. Selenium anomalous maps used to phase LmrP data. Methionine residues are shown as sticks, and anomalous maps collected at the selenium edge, contoured at 3 σ, are shown in green.

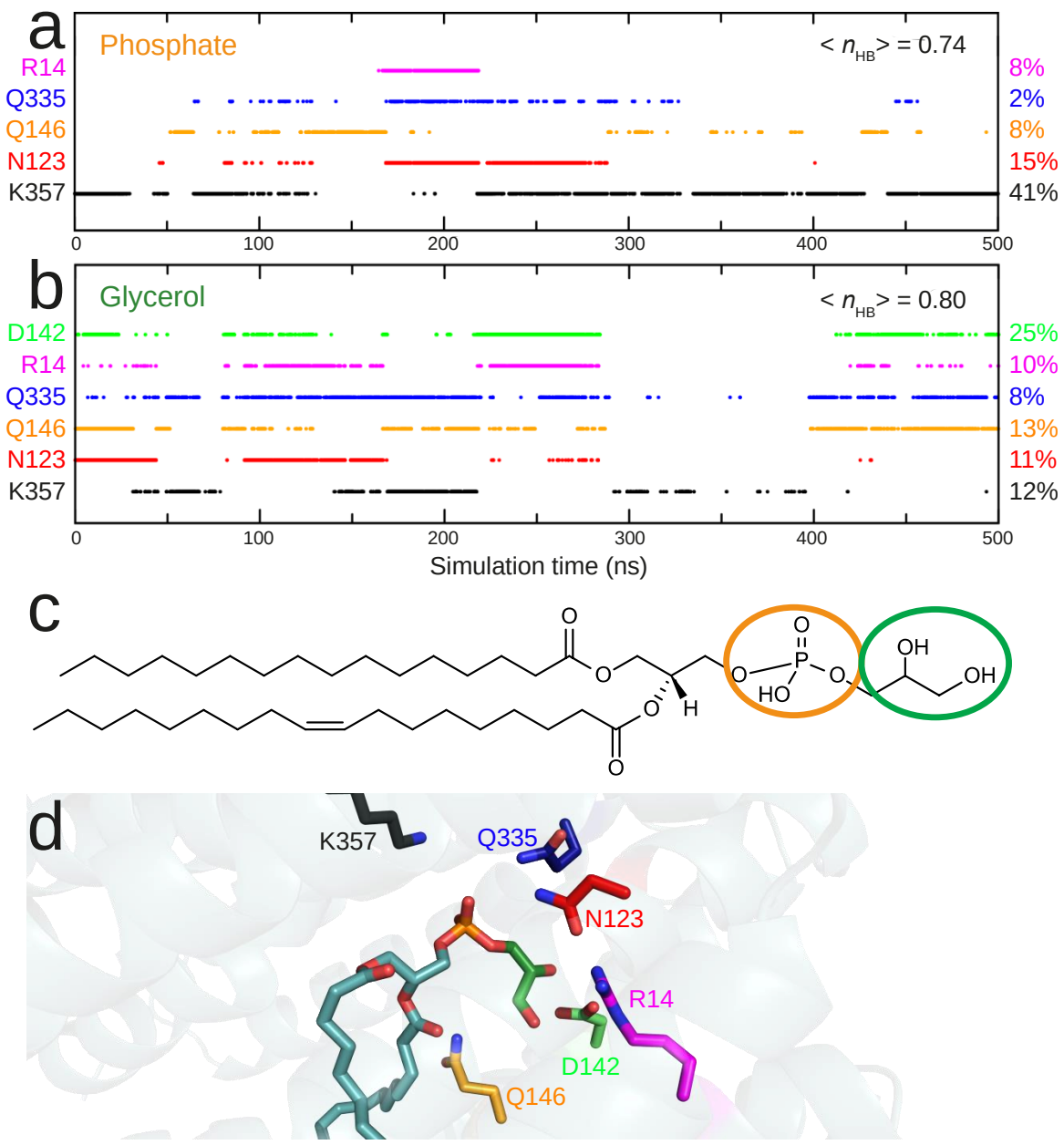

Supplementary Figure 3. Hydrogen-bonding interactions between POPG and outward-facing LmrP. Plots indicating observed hydrogen-bonds between either the phosphate group in POPG (a) or the glycerol within the headgroup (b) and surrounding polar side-chains in LmrP, as a function of simulation time. Each dot (coloured according to the residue label) reflects an observed interaction. c) A diagram of POPG highlighting the relevant phosphate and headgroup glycerol. d) A molecular dynamics simulation snapshot demonstrating the positions of each interacting residue relative to the lipid.

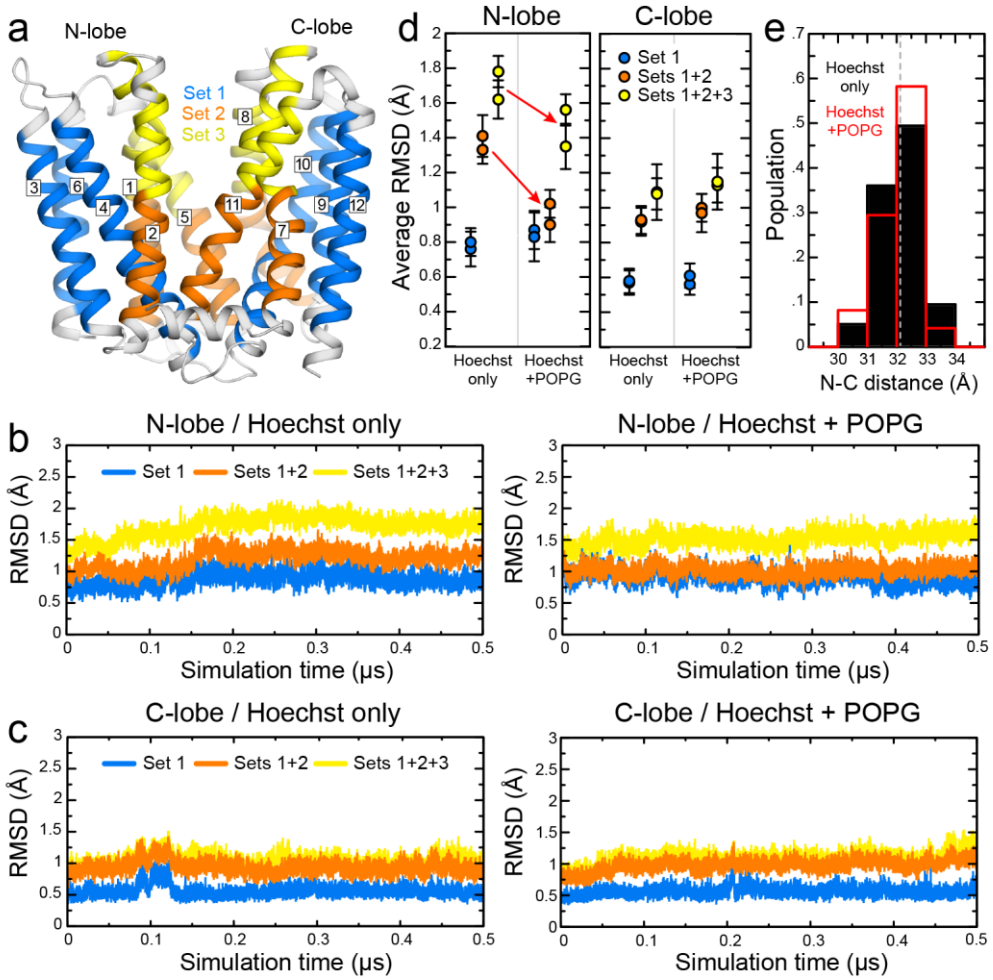

Supplementary Figure 4. Molecular dynamics simulations of the LmrP-Hoechst complex with and without POPG bound. a) View of outward-facing LmrP along the membrane plane, with structural regions of seemingly distinct dynamics colour-coded. Ligands are omitted for clarity. The peripheral regions, or Set 1 (blue), comprise TM helices 3, 4 and 6 in the N-lobe and TM 9, 10 and 12 in the C-lobe. Set 2 (orange) comprises the intracellular half of TM helices 1, 2 and 5, and TM 7, 8 and 11, respectively. Set 3 (yellow) includes the remainder of these 6 helices. b) Analysis of the structural dynamics of the N-lobe in terms of the root-mean-square deviation of the protein backbone relative to the X-ray structure (after least-squares self-fit). For each of the regions defined in (a) (Sets 1, 1+2 or 1+2+3), the plot shows the evolution of RMSD as a function of simulation time. Left and right plots compare simulations with only Hoechst bound to LmrP, and with both Hoechst and POPG bound, respectively. For clarity, only one of the two trajectories calculated in each case is analysed. c) Same as (b), for the C-lobe. d) Summary of the RMSD time-series data, in terms of time-averages alongside the corresponding standard deviations, for two independent simulations of each system. Data are compared for simulations of LmrP bound to Hoechst 33342, and of LmrP bound to Hoechst and a POPG lipid. Red arrows indicate regions for which a significant change was observed between simulation systems. e) Dynamics of the N- and C-lobes relative to each other, in the presence or absence of bound POPG. The plot quantifies the variability in distance between the two lobes, defined as the distance between the centres-of-mass of the peripheral regions in each lobe (Set 1, blue). The histograms shown derive from the time-series of this distance, combining the two simulations calculated with and without bound POPG. The value of this distance in the LmrP crystal structure is also indicated (vertical grey dashed line).

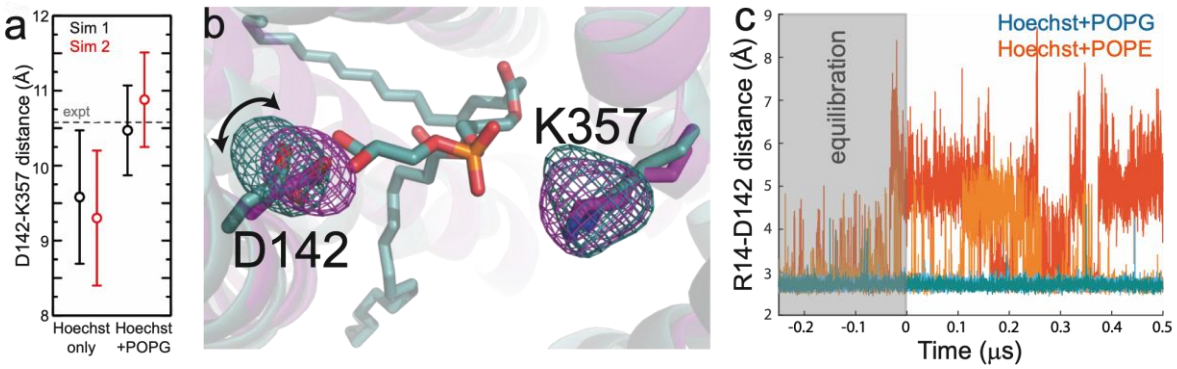

Supplementary Figure 5. An embedded POPG helps stabilise charged residues within the binding pocket during molecular dynamics simulations. a) Minimum distance between D142 (atoms $O_{\delta 1}$, $O_{\delta 2}$) and K357 (atom N_z). The plot compares the value of this distance in the crystal structure (horizontal grey dashed line) with time-averages calculated from the final 100 ns of the simulations of LmrP-Hoechst and those of LmrP-Hoechst-POPG. Error bars denote the standard deviations of the time-averages. b) 3D mass-density maps of D142 and K357 from simulations with only Hoechst 33342 (magenta), and from simulations with Hoechst 33342 and POPG (teal) highlight the difference in position of D142 in the absence of POPG. The conformations of D142 and K357 at the end of each simulation are shown as a visual aid. c) In simulations with POPG present (teal and cyan) the distance between R14 and D142 is consistent with that observed in the crystal structure. When POPE is modelled instead of POPG (light orange and dark orange), the R14-D142 salt-bridge breaks off, as observed when no lipid is modelled (Figure 3d), but in the simulated timescale R14 remains within the binding cavity. Two independent trajectories for each simulation condition are shown.

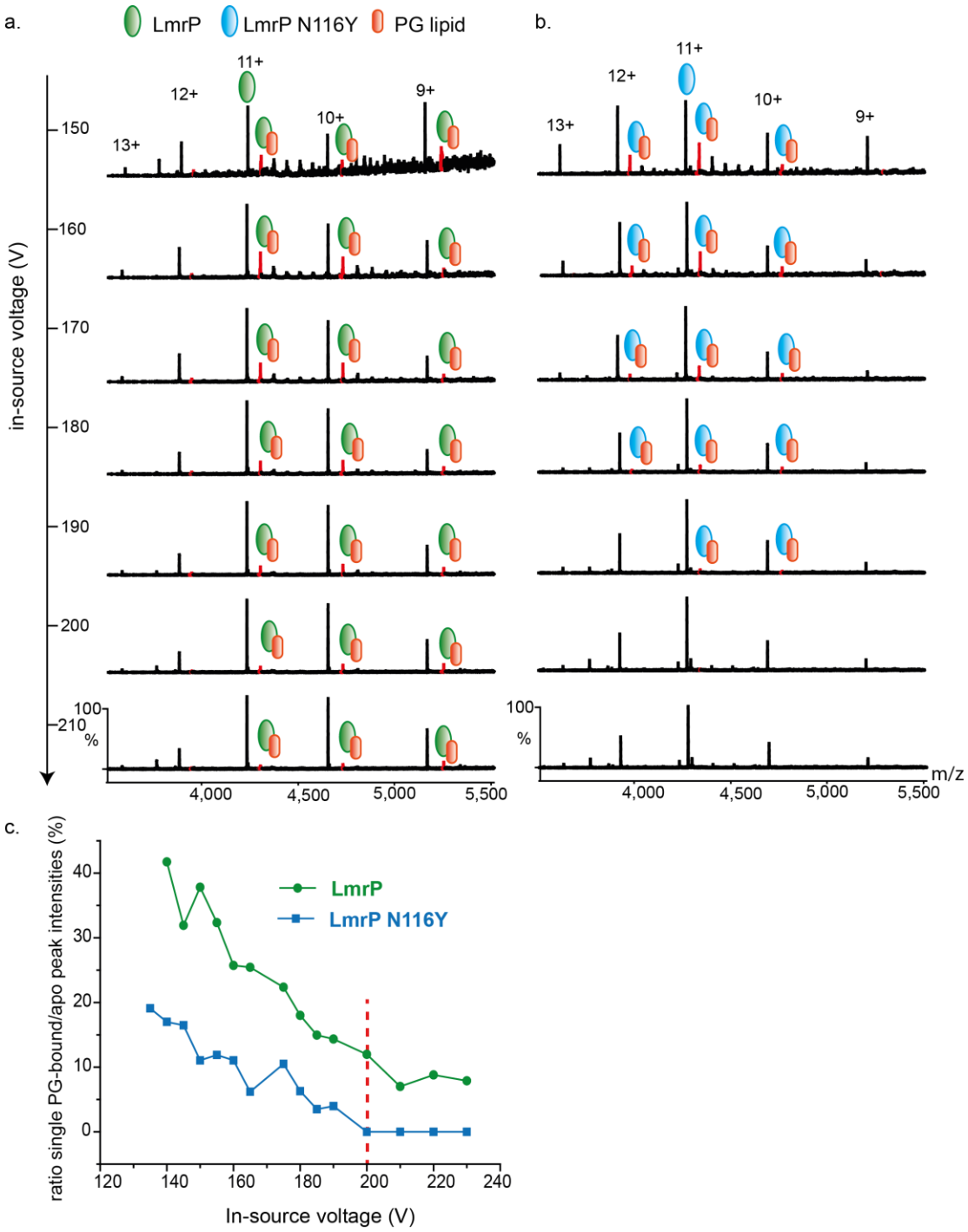

Supplementary Figure 6. Native MS identifies a specific interaction between LmrP and PG phospholipid inside the binding pocket cavity. Mass spectra recorded at increasing energies by modulating in-source trapping voltage values for (a) LmrP and (b) LmrP N116Y reconstituted in PE:PG nanodiscs (80:20). c) A plot of the relative fractional intensity of the single PG-bound LmrP peak versus the LmrP apo peak over increasing source voltage values. The individual mass spectra at each voltage value were transformed using the MaxEnt 1 deconvolution algorithm and the peak intensities of both bound and unbound species were extracted. The red dashed line indicates the voltage value where no PG lipid is observed on the mutant anymore.

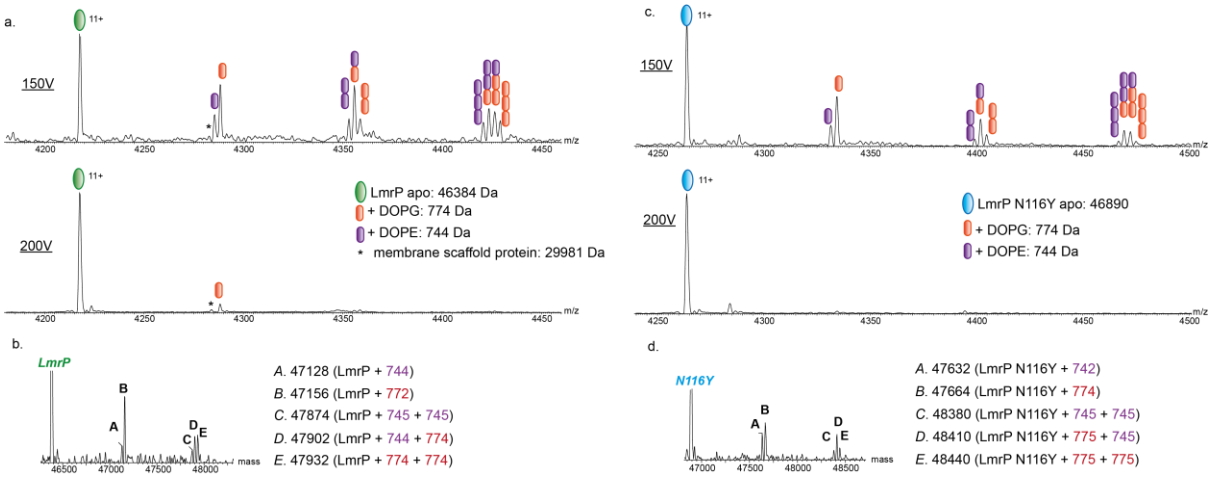

Supplementary Figure 7. High resolution nMS analysis differentiates lipid adducts on LmrP. a) Zoom-in of the 11+ charge state of the high-resolution Orbitrap mass spectrum of LmrP in DOPE:DOPG MSP-based nanodiscs, obtained at 150V (upper panel) and 200V (lower panel) in-source voltage. The number and identity of lipid adducts is indicated for each peak, with the orange and purple ovals indicating DOPG and DOPE binding respectively. b) Deconvoluted mass spectrum of LmrP obtained at 150V in-source voltage. The exact masses of each peak are indicated and allow identification of the exact pattern of bound lipids. c) Zoom-in of the 11+ charge state of the high-resolution Orbitrap mass spectrum of LmrP N116Y mutant in DOPE:DOPG MSP-based nanodiscs, at 150V (upper panel) and 200V (lower panel) in-source voltage. d) Deconvoluted mass spectrum of LmrP N116Y obtained at 150V in-source voltage. Deconvolution was performed using the MaxEnt1 deconvolution algorithm.

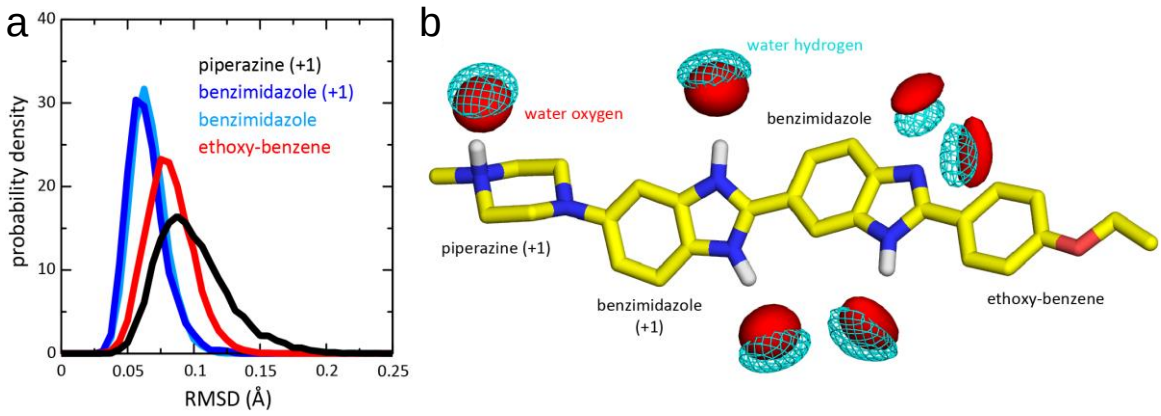

Supplementary Figure 8. MD simulation of Hoechst 33342 in solution, using the newly-developed CHARMM-compatible forcefield. a) Comparison of the geometry of Hoechst 33342 in simulation and the experimental structure observed in complex with LmrP, in terms of the RMS difference between simulated and experimental geometries for each of the constituent chemical groups. The RMSD data is shown as histograms, derived from time-series of 100 ns. b) Evaluation of the interaction of Hoechst with water. For each snapshot in a 100-ns trajectory, water molecules in the first hydration shell were mapped onto a 3D number-density distribution (oxygen and hydrogen atoms separately), which was then time-averaged. Iso-density surfaces/meshes are shown for water oxygen (red, 0.07 σ) and hydrogen (cyan, 0.14 σ), to highlight the most persistent interaction sites and relative ligand-water orientations.